

1 Supporting information for:

2  
3 Kinetics and impacting factors of HO<sub>2</sub> uptake onto submicron atmospheric aerosols during a  
4 2019 air quality study (AQUAS) in Yokohama, Japan

5 Jun Zhou<sup>a,b,c,\*</sup>, Kei Sato<sup>d</sup>, Yu Bai<sup>e</sup>, Yukiko Fukusaki<sup>f</sup>, Yuka Kousa<sup>f</sup>, Sathiyamurthi  
6 Ramasamy<sup>d</sup>, Akinori Takami<sup>d</sup>, Ayako Yoshino<sup>d</sup>, Tomoki Nakayama<sup>g</sup>, Yasuhiro Sadanaga<sup>h</sup>,  
7 Yoshihiro Nakashima<sup>i</sup>, Jiaru Li<sup>c</sup>, Kentaro Murano<sup>c</sup>, Nanase Kohno<sup>c</sup>, Yosuke Sakamoto<sup>c,d,e</sup>,  
8 Yoshizumi Kajii<sup>c,d,e,\*</sup>

9 <sup>a</sup>Institute for Environmental and Climate Research, Jinan University, 511443 Guangzhou, China

10 <sup>b</sup>Guangdong-Hongkong-Macau Joint Laboratory of Collaborative Innovation for Environmental Quality,  
11 Guangzhou 511443, China.

12 <sup>c</sup>Graduate School of Global Environmental Studies, Kyoto University, Kyoto, 606-8501, Japan

13 <sup>d</sup>Center for Regional Environmental Research, National Institute for Environmental Studies, Tsukuba,  
14 Ibaraki 305-8506, Japan

15 <sup>e</sup>Graduate School of Human and Environmental Studies, Kyoto University, Kyoto 606-8501, Japan

16 <sup>f</sup>Yokohama Environmental Science Research Institute, Yokohama Kanagawa 221-0024, Japan

17 <sup>g</sup>Faculty of Environmental Science and Graduate School of Fisheries and Environmental Sciences, Nagasaki  
18 University, Nagasaki 852-8521, Japan

19 <sup>h</sup>Graduate School of Engineering, Osaka Prefecture University, Sakai, Osaka 599-8531, Japan

20 <sup>i</sup>Graduate School of Agriculture, Tokyo University of Agriculture and Technology, 3-5-8 Saiwai-cho, Fuchu,  
21 Tokyo 183-8538, Japan

22 E-mail address: kajii.yoshizumi.7e@kyoto-u.ac.jp and junzhou@jnu.edu.cn

23

24

25 The Supporting Information includes the following contents and Figures.

26

27 **Contents**

28 Air mass directions iii

29 Measurement strategy vii

30 A technique combined laser-flash photolysis with laser-induced fluorescence (LFP–LIF) viii

31 The enrichment of the ambient aerosols ix

32 HO<sub>2</sub> reactivity of ambient air x

33 Correction of gas-phase diffusion for HO<sub>2</sub> uptake coefficient xii

34 HO<sub>2</sub> reactivity of ambient gas phase ( $k_g$ ) xiii

35 Temperature and pressure influence correction xiv

36 Profiles of key factors used in Section 3.5: xviii

37 References xxi

38

39 **Figures**

40

41 Figure S1: NOAA-HYSPLIT model showing back trajectories for ~ 11 days sample periods from 12:00  
42 July 24 to 00:00 August 04, 2019 (back trajectories ending 00:00 UTC 25 July to 00:00 August 04,  
43 2019) from the sampling site. Arriving air masses 250 m, 500 m, and 1000 m above ground level (AGL)  
44 were calculated using the following website: [http://ready.arl.noaa.gov/hypub-  
bin/trajtype.pl?runtype=archive](http://ready.arl.noaa.gov/hypub-<br/>45 bin/trajtype.pl?runtype=archive) ..... vii

46

47 Figure S2: (a) Sampling setup for testing HO<sub>2</sub> reactivity using laser-flash photolysis and laser-induced  
48 fluorescence (LFP–LIF) with a versatile aerosol concentration enrichment system (VACES) and auto-  
49 switching aerosol filter (SMPS = scanning mobility particle sizer; AMS = aerosol mass spectrometer;  
50 CAPS=cavity attenuated phase shift). (b) Detailed presentation of the measurement process of the HO<sub>2</sub>  
51 reactivity of the ambient aerosol phase. Further details concerning the measurement process can be  
52 found in our previous publication<sup>3</sup> .....viii

53

54 Figure S3: Examples of the measured HO<sub>2</sub> decay profiles in zero air (black lines), ambient air without  
55 aerosol phase (green lines), and ambient air with enriched aerosol phase (red lines) at an RH of ~60%,  
56 301 K, and an initial HO<sub>2</sub> concentration of ~10<sup>10</sup> molecules cm<sup>-3</sup>. The log scale plot in the inserted  
57 figure at the upper right shows linear fitting in the range 0.08–0.4. ....xii  
58

59 Figure S4: Average of HO<sub>2</sub> reactivity calibrations using LFP–LIF with different NO<sub>2</sub> concentrations  
60 supplied by NO<sub>2</sub> gas. The green lines represent the ±68.3% prediction band of the calibration data points  
61 (1σ = 0.1 s<sup>-1</sup>), i.e., the uncertainty in the estimation of HO<sub>2</sub> reactivity using the calibration curve. ...xiii

62 Figure S5: Diurnal trends in non-refractory chemical components plus eBC of group i (left side) and  
63 group ii (right side). ....xv

64 Figure S6: Diurnal trends in total HO<sub>2</sub> reactivity caused by the ambient aerosol phase (*k<sub>a</sub>*, upper panel)  
65 and the HO<sub>2</sub> uptake coefficients onto ambient aerosols (*γ*, lower panel). ....xv

66 Figure S7: Correlations between measured and modeled *γ* with (a) *γ* < 0.4 and (b) *γ* ≥ 0.4. ....xvi

67 Figure S8: Time series of the half an hour averaged ambient RH (red open cycles in the upper panel)  
68 and temperature (red filled cycles in the lower panel) measurements in comparison to the reaction cell  
69 RH (black open cycles in the upper panel) and temperature (black filled cycles in the lower panel)...xvi

70 Figure S9: *k<sub>a</sub>* and *γ* values as a function of RH in the reaction cell, colored coded with *T*. ....xvii

71 Figure S10: *k<sub>a</sub>* (upper panel) and *γ* (lower panel) as a function of mean particle diameter, color coded  
72 with the surface area concentration. ....xvii

73 Figure S11: Dependence of day time LN/Q and LN/Q\_without\_aerosol on [NO]. ....xviii

74 Figure S12: Temporal variations in key factors in ambient air for determining XO<sub>2</sub> loss rates and P(O<sub>3</sub>)  
75 sensitivity in Sect. 3.6. ....xix

76

77 **Tables**

78

79 Table S1: Summary of equations and values used in section 3.4. ....xviii

80 Table S2: Summary of equations and values used in section 3.6. ....xvii

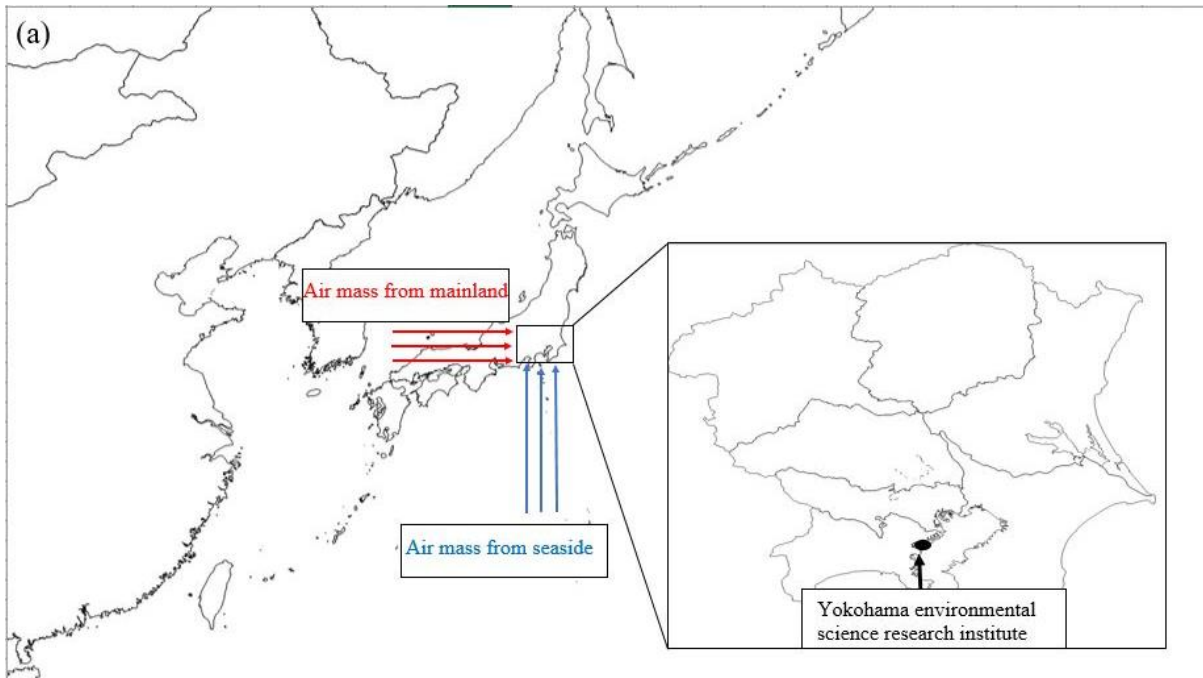
81

82

83 **Air mass directions**

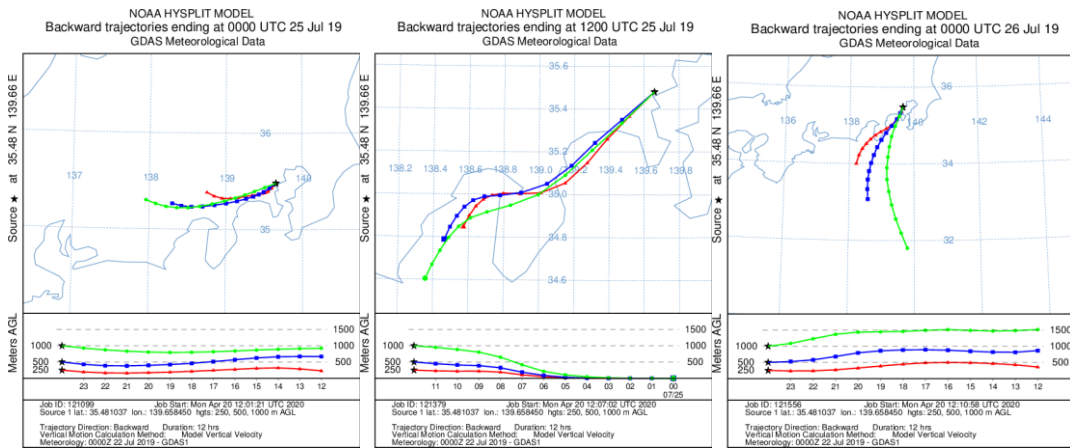
84 Figure S1a shows air mass direction schematic diagram during the campaign. For each day, the  
85 Internet-Based HYSPLIT Trajectory Model and gridded meteorological data (Global Data Assimilation  
86 System, GDAS1) from the U.S. National Oceanic and Atmospheric Administration (NOAA) were used  
87 during the modeling, the tested results of all experimental days are listed in Fig. S1b. Backward

88 trajectories ended at local time 00:00 am and 12:00 pm after a total run time of 12 h. Results suggesting  
89 that arriving air mass can be classified into two categories (i) from the sea to the north direction towards  
90 Yokohama City (~19% of the experimental period: from 12:00 pm Jul. 25 to 12:00 Jul. 27, 2019); (ii)  
91 from the mainland towards Yokohama City (~81% of the experimental period).

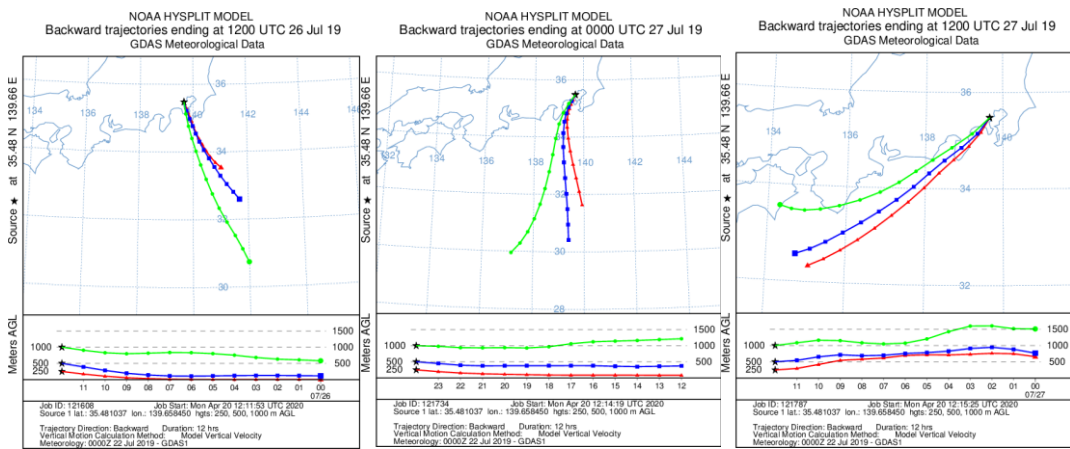


92  
93  
94  
95  
96  
97  
98  
99  
100  
101  
102  
103  
104  
105

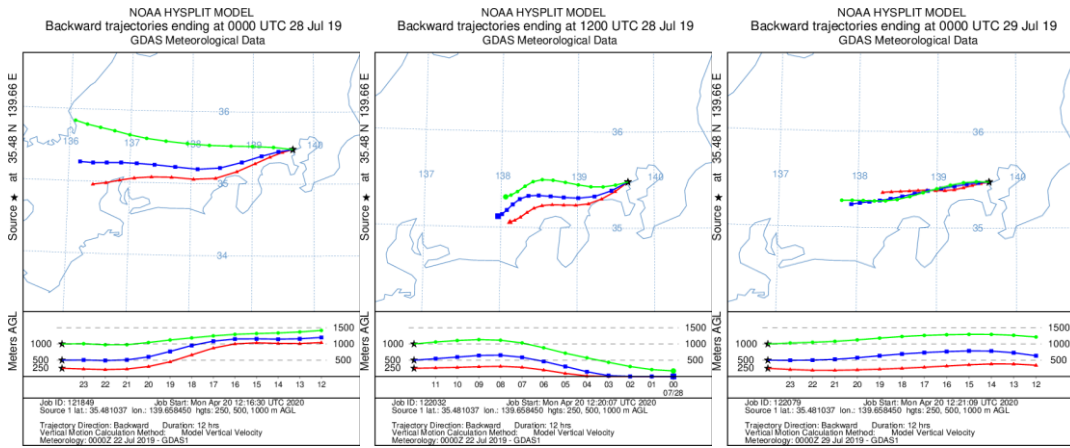
106 (b)



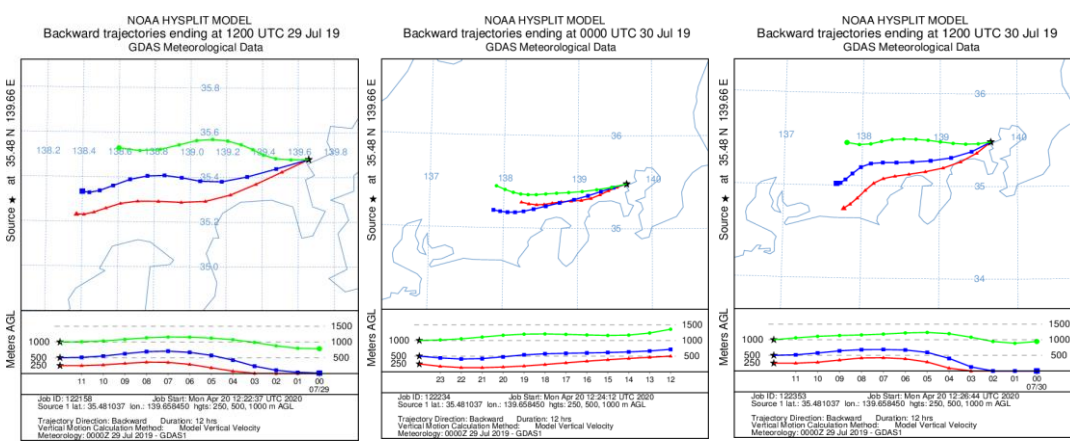
107



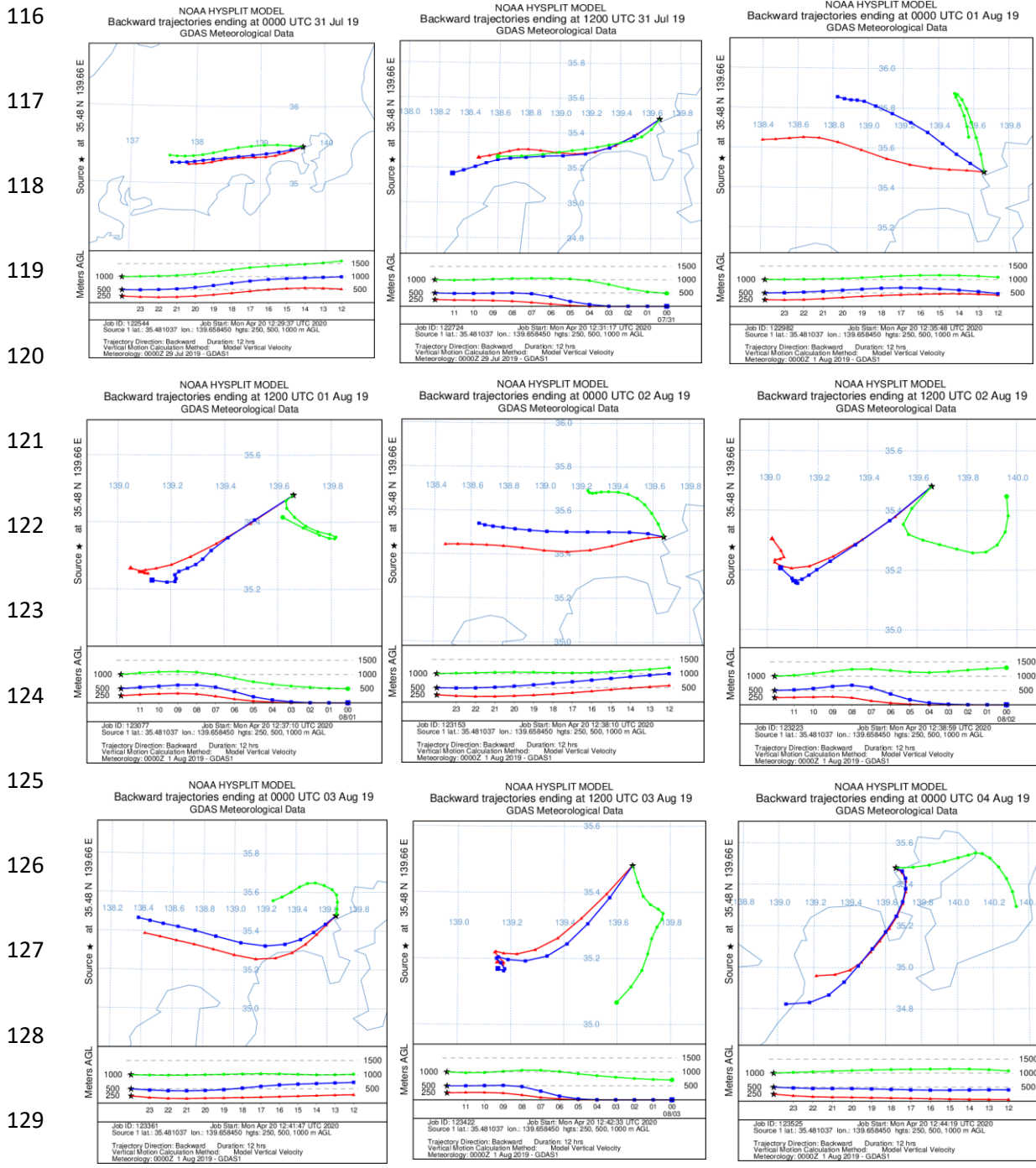
108



109



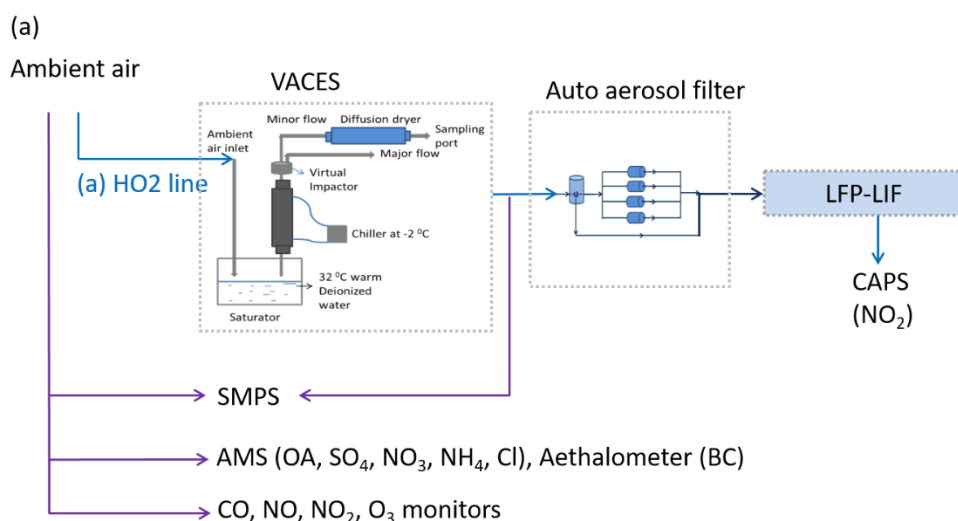
115



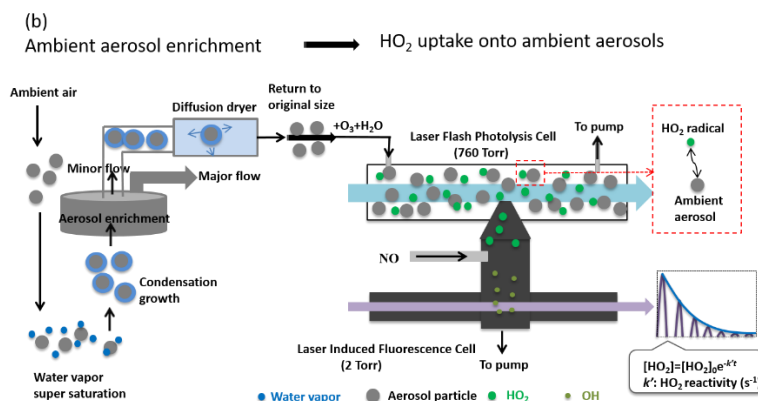
130 Figure S1: (a) Air mass direction schematic diagram; (b) NOAA-HYSPLIT model showing back  
 131 trajectories for ~ 11 days sample periods from 12:00 July 24 to 00:00 August 04, 2019 (back trajectories  
 132 ending 00:00 UTC 25 July to 00:00 August 04, 2019) from the sampling site. Arriving air masses 250  
 133 m, 500 m, and 1000 m above ground level (AGL) were calculated using the following website:  
 134 <http://ready.arl.noaa.gov/hypub-bin/trajtype.pl?runtype=archive>

136 **Measurement strategy**

137 The HO<sub>2</sub> reactivity was measured using LFP-LIF, adapted from a laser-induced pump and probe OH  
138 reactivity measurement technique, which has been validated and employed for the total gas phase HOx  
139 (=OH+HO<sub>2</sub>) reactivity and HOx uptake kinetics onto ambient aerosols in field<sup>1, 2-4</sup>. We further coupled  
140 this system with a versatile aerosol concentration enrichment system (VACES) to enrich the ambient  
141 aerosols to compensate the relatively low limit of detection (LOD) for the HO<sub>2</sub> reactivity measurement.  
142 A schematic of the experimental system is shown in Fig. S2a, and a detailed abstract of the measurement  
143 process of the HO<sub>2</sub> reactivity of the ambient aerosol phase is shown in Fig. S2b. The ambient air was  
144 drawn into the VACES, where the aerosol concentration was enriched. The ambient air was then  
145 sampled using a three-port valve (Bolt, Flon Industry Co., LTD) and injected into the LFP-LIF system  
146 at a flow rate of 10 L min<sup>-1</sup>. The valve was switched automatically between two sampling lines, one  
147 with the aerosol filter and the other without the aerosol filter (termed “the auto-switching aerosol filter”  
148 hereafter), which enabled alternative measurements of HO<sub>2</sub> reactivity by the gas phase and the gas +  
149 enriched aerosol phase of the ambient air, separately.



150



151

152 Figure S2: (a) Sampling setup for testing HO<sub>2</sub> reactivity using laser-flash photolysis and laser-induced  
 153 fluorescence (LFP–LIF) with a versatile aerosol concentration enrichment system (VACES) and auto-  
 154 switching aerosol filter (SMPS = scanning mobility particle sizer; AMS = aerosol mass spectrometer;  
 155 CAPS = cavity attenuated phase shift); and (b) Detailed presentation of the measurement process of the  
 156 HO<sub>2</sub> reactivity of the ambient aerosol phase. Further details concerning the measurement process can  
 157 be found in our previous publication<sup>3</sup>.

### 158 A technique combined laser-flash photolysis with laser-induced fluorescence (LFP–LIF)

159 LFP–LIF comprises two cells: the laser-flash photolysis cell (the reaction cell) and the laser-induced  
 160 fluorescence detection cell (the detection cell). In the HO<sub>2</sub> reaction cell, pure air was supplied by a zero-  
 161 air generator (Model 111, Thermo Fisher Scientific Inc., USA), and relative humidity was controlled by  
 162 bubbling water vapor into one part of the zero air. The ambient air was sampled into the reaction cell  
 163 after mixed with the humidified zero air and O<sub>3</sub>, where O<sub>3</sub> (~100 ppb) was generated by 184.9 nm  
 164 irradiation of zero air by a low-pressure Hg lamp (pen ray lamp, Sen lights corporation, JP, part number:  
 165 SP-5-2H (5w)) at 50 sccm (standard cubic centimeter per minute, at 273 K and 1 atm). The reaction cell  
 166 was made of aluminum, with a length of 1.4 m and an inner diameter of 0.04 m, and the inner wall of  
 167 the flow tube was coated with Teflon to reduce the heterogeneous losses of HO<sub>2</sub> and the reactants. The  
 168 sample inlet of the detection cell was located ~0.7 m from the sample injection position. The total flow  
 169 inside the reaction cell was ~10 L min<sup>-1</sup>, with a residence time of ~4.8 s. The Reynolds number in the  
 170 reaction cell was ~354 and (1 atm pressure and 298 K were assumed inside the reaction cell), thus  
 171 indicating a laminar flow. A pulsed 266-nm Nd:YAG laser (Tempest 300, New Wave Research Inc.,  
 172 USA), with a 1-cm diameter, laser power ranging between 0.4 and 3.0 mJ pulse<sup>-1</sup>, and a repetition of 1  
 173 Hz, was used in the reaction cell to irradiate the sample air to produce OH through reactions SR1–SR2.



176 Meanwhile, excess CO was introduced into the reaction cell to convert all OH radicals to HO<sub>2</sub>:



179 The initial HO<sub>2</sub> concentration in the reaction cell was of the order of 10<sup>10</sup> molecules cm<sup>-3</sup>, estimated  
180 from the photolysis power, humidity, and O<sub>3</sub> concentration<sup>3</sup>. A stream of flow (~ 2 LPM) in the reaction  
181 cell was pumped into the detection cell using a rotary oil pump (D-950, ULVAC) under a pressure of  
182 1.6 Torr through a 0.5-mm pinhole. NO (>99.999%) was injected with a flow rate of 3 sccm between  
183 the reaction cell and the detection cell to convert HO<sub>2</sub> to OH (Eq. SR5, conversion efficiency: ~ 30%).  
184 The second harmonic of a pulsed laser (Sirah Credo, Spectra Physics) pumped by the second harmonic  
185 of a Nd:YVO<sub>4</sub> laser (YHP40-532Q, Spectra Physics) and set at a maximum absorption of Q<sub>1</sub>(2) A<sup>2</sup>Σ<sup>+</sup>(v'  
186 = 0) ← X<sup>2</sup>Π<sub>3/2</sub>(v'' = 0) transition of OH at 308 nm was used to irradiate the detection cell with a  
187 repetition rate of 10 kHz. The fluorescence emitted by the OH radical induced by each irradiation was  
188 collected by a photomultiplier tube (R2256P, Hamamatsu Photonics), and a decay file of OH was  
189 obtained after 240 integrations. The HO<sub>2</sub> decay rate was considered the same as the OH decay rate as  
190 we were measuring the relative change in the HO<sub>2</sub> concentration in the detection cell.



## 192 **The enrichment of the ambient aerosols**

193 The versatile aerosol concentration enrichment system (VACES) was built according to Sioutas  
194 et al. (1999)<sup>5</sup>, which comprises the aerosol growth part and the aerosol enrichment part (as shown in  
195 Fig. S2a). The ambient air sample was drawn into VACES at a flow rate of over 100 L min<sup>-1</sup> (Q<sub>tot</sub>) into  
196 a ultra-pure water tank which was heated to ~32°C, where the ambient air steam was saturated and then  
197 cooled down in a condenser connected immediately above the tank (with a temperature of -2 °C). The  
198 grew ambient aerosol (mostly with a diameter > 2 μm) through condensed water droplets were then

199 enriched by a virtual impactor with a 50% cutoff point less than 1  $\mu\text{m}$ , with  $\sim 90 \text{ L min}^{-1}$  going to the  
200 major flow that connected to the exhaust pump and  $\sim 10 \text{ L min}^{-1}$  going to the minor flow ( $q_{\text{min}}$ ) that  
201 connected to the aerosol instrumentations after passing through a diffusion dryer. In theory, the  
202 enrichment factor (EF) of the ambient aerosol concentration can be estimated as:

$$203 \quad \text{EF} = Q_{\text{tot}}/q_{\text{min}}(1 - \text{WL}) \times \eta_{\text{vi}} \quad (\text{S1})$$

204 where  $\eta_{\text{vi}}$  and WL are its collection efficiency and fractional loss, respectively<sup>5</sup>. The enrichment  
205 efficiency (EE) of the impactor was estimated as  $\sim 1^3$ . In this study, we test the enrichment factor of the  
206 surface area of the enriched ambient aerosols ( $E$ ) by connecting two SMPS before and after VACES  
207 separately for  $\sim 2$  hours every day for  $\sim 6$  days, the enrichment factor can be calculated as:

$$208 \quad E = \frac{S1}{S2} \quad (\text{S2})$$

209 Where S1 and S2 are the surface areas of the enriched ambient aerosols after VACES and the ambient  
210 aerosols before VACES, respectively. Obtained  $E$  values from all the tests were then averaged and used  
211 as the final enrichment factor ( $\sim 12.5$ ) for all the experimental days.

## 212 **HO<sub>2</sub> reactivity of ambient air**

213 Owing to the excess CO, almost all HO<sub>2</sub> radicals formed in the reaction cell after the photolysis pulse,  
214 and the HO<sub>2</sub> and RO<sub>2</sub> radicals in urban ambient air were destroyed, or at least partially, during their  
215 intake into the LFP detection cell, thus the self-reaction of HO<sub>2</sub> and the interaction of HO<sub>2</sub> with RO<sub>2</sub>  
216 owing to the inherent HO<sub>2</sub>/RO<sub>2</sub> concentrations from ambient air was negligible. Due to the large excess  
217 reactants over HO<sub>2</sub> radicals produced in the LFP reaction cell, pseudo-first order conditions were  
218 achieved, and the HO<sub>2</sub> decay rate  $k$  (HO<sub>2</sub> reactivity) can be explained through the following equation<sup>2</sup>:

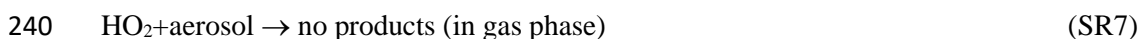
$$219 \quad \frac{d[\text{HO}_2]}{dt} = -(k_{\text{NO}_2}[\text{NO}_2] + k_{\text{NO}}[\text{NO}] + k_{\text{aerosol}}[\text{ambient aerosol}] + k_{\text{wall}}) \times [\text{HO}_2] \quad (\text{S3})$$

220 where  $k_i$  is the rate constant of the HO<sub>2</sub> reaction with different reacting species  $i$ , where  $i = \text{NO}_2, \text{NO}$   
221 and the ambient aerosols.  $k_{\text{wall}}$  is the loss rate of the HO<sub>2</sub> radicals onto the wall, and  $[i]$  represents the  
222 concentration of the reacting species  $i$ . Due to the short reaction time,  $k_{\text{wall}}$  was small and included in

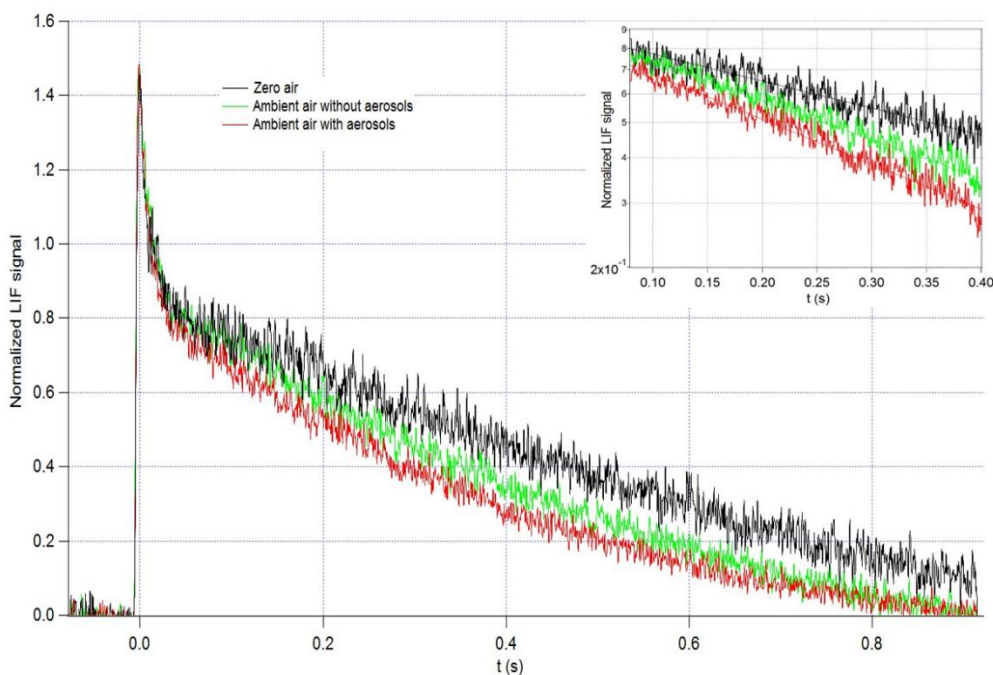
223 the baseline. And the consumption of HO<sub>2</sub> by NO in the reaction cell is immediately compensated by  
224 excess CO, converting its product OH back to HO<sub>2</sub>; therefore, the HO<sub>2</sub> decay in the LFP reaction cell  
225 may be mostly attributed to its reaction with NO<sub>2</sub> and aerosol phase. The reaction with NO<sub>2</sub> will produce  
226 peroxyntic acid:



228 Ideally, the thermal unimolecular decomposition of HO<sub>2</sub>NO<sub>2</sub> may occur. However, we didn't consider  
229 this reverse reaction, due to (1) The reaction cell (~40 mm diameter) is considerably larger than the  
230 reaction-initialized region (the laser beam covered area, ~10 mm diameter). The HO<sub>2</sub>, NO<sub>2</sub>, and  
231 HO<sub>2</sub>NO<sub>2</sub> that are produced will diffuse to the outside of the reaction-initialized region (~16 times  
232 diluted), thus largely reducing the reactant concentrations. Further, reproducing the reaction process is  
233 impossible because the sampling port of the deflection cell is located in the center of the reaction-  
234 initialized region; (2) The log scale plot of the HO<sub>2</sub> decay profile as a function of time was linear in the  
235 fitting range (as illustrated in Fig. S3). 3) As shown in Fig. S4, the HO<sub>2</sub> reactivity exhibited a linear  
236 correlation with the wide concentration range of NO<sub>2</sub>. These phenomena indicate the negligible  
237 influence of the reverse reaction to the gas phase HO<sub>2</sub> reactivity. We also observed the negligible reverse  
238 reaction previously, even in the case of lower HO<sub>2</sub> and NO<sub>2</sub> concentrations<sup>2</sup>. We assume the  
239 heterogeneous loss of HO<sub>2</sub> by the aerosol following the single first order reaction step as:



241 HO<sub>2</sub> was converted to OH in the reaction with NO in the detection cell, according to Eq. SR5. The HO<sub>2</sub>  
242 concentrations were then measured by laser-induced fluorescence from OH after each probe laser (266  
243 nm) irradiation to obtain a decay curve. Examples of the time series of HO<sub>2</sub> decay files of zero air,  
244 ambient air without aerosols and ambient air with enriched aerosols are shown in Fig. S3.



245

246 Figure S3: Examples of the measured HO<sub>2</sub> decay profiles in zero air (black lines), ambient air without  
 247 aerosol phase (green lines), and ambient air with enriched aerosol phase (red lines) at an RH of ~60%,  
 248 301 K, and an initial HO<sub>2</sub> concentration of ~10<sup>10</sup> molecules cm<sup>-3</sup>. The log scale plot in the inserted  
 249 figure at the upper right shows linear fitting in the range of 0.08–0.4.

### 250 Correction of gas-phase diffusion for HO<sub>2</sub> uptake coefficient

251  $\gamma_{obs}$  includes the gas phase diffusion, and as the HO<sub>2</sub> radical is active in aerosol bulk, the resistance  
 252 model was usually utilized for explaining the observed uptake coefficients (George et al., 2013;  
 253 Davidovits et al., 2006):

$$254 \quad \frac{1}{\gamma_{obs}} = \frac{1}{\gamma_{diffusion}} + \frac{1}{\alpha} + \frac{1}{\gamma_{reaction+partitioning}} \quad (S4)$$

255 where  $\gamma_{obs}$  and  $\gamma_{diffusion}$  represent the observed uptake coefficients and the gas transport coefficient,  
 256 respectively,  $\alpha$  is the mass accommodation, and the third term represents the resistance caused by the  
 257 sum of the reactive and partitioning processes within the aerosol. The observed uptake coefficients were  
 258 further corrected to take into account gas diffusion contribution, and the final  $\gamma$  can be obtained from  
 259 Eq. S5<sup>6, 7</sup>:

$$260 \quad \gamma = \frac{\gamma_{obs}}{1 - \gamma_{obs}\lambda(r_s)} \quad (S5)$$

261 where  $\lambda(r_s)$  are is obtained from Eq. S10:

262 
$$\lambda(r_s) = \frac{0.75+0.283K_n}{K_n(1+K_n)} \quad (S6)$$

263 where  $K_n = \frac{3D_g}{w_{HO_2}r_s}$  (S7)

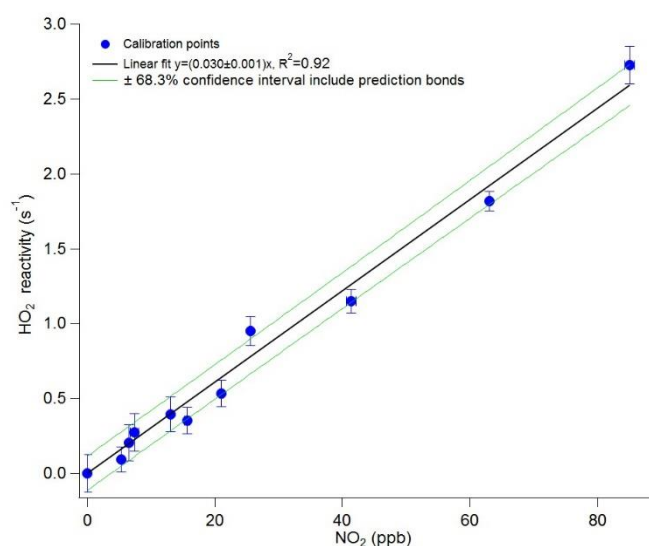
264 where  $D_g$  is the gas phase diffusion coefficient of  $HO_2$  ( $0.25 \text{ cm}^2 \text{ s}^{-1}$ ) at  $\sim 298 \text{ K}$ , and  $r_s$  represents the  
 265 average radius of the aerosols, defined as follows:

266 
$$r_s^2 = \frac{A_{total}}{4\pi N_{total}} \quad (S8)$$

267 where  $A_{total}$  denotes the total surface area measured and  $N_{total}$  denotes the total number of particles  
 268 producing that surface area.

269  **$HO_2$  reactivity of ambient gas phase ( $k_g$ )**

270 Gas phase  $HO_2$  reactivity was directly measured in the reaction cell without aerosol phase. To check  
 271 the dominant factor of the gas phase  $HO_2$  reactivity, we modeled the  $HO_2$  reactivity by using the  $NO_2$   
 272 concentration in the LFP reaction cell, using the calibration factor obtained by plotting the measured  
 273  $HO_2$  decay rates as a function of the  $NO_2$  concentration prepared in the laboratory (with the  $NO_2$   
 274 concentration in zero air ranging from 0 to 85 ppb at 298 K and 1 atm in the reaction cell, Fig. S4).



275  
 276 Figure S4: Average of  $HO_2$  reactivity calibrations using LFP–LIF with different  $NO_2$  concentrations  
 277 supplied by  $NO_2$  gas. The green lines represent the  $\pm 68.3\%$  prediction band of the calibration data points  
 278 ( $1\sigma = 0.1 \text{ s}^{-1}$ ), i.e., the uncertainty in the estimation of  $HO_2$  reactivity using the calibration curve.

279 The linear fitting coefficient represents the HO<sub>2</sub> reactivity with NO<sub>2</sub> concentrations in the reaction cell,  
 280 which was 0.030 s<sup>-1</sup> ppb<sup>-1</sup> with a standard deviation of 0.001. This indicates that the instrument accuracy  
 281 in determining  $k_{\text{HO}_2}$  from NO<sub>2</sub> concentration was 3%. This calibration factor was used to simulate HO<sub>2</sub>  
 282 reactivity ( $k_{\text{HO}_2}$ ) caused by NO<sub>2</sub> from ambient air in the LIF reaction cell as follows:

$$283 \quad k_{\text{HO}_2}(\text{s}^{-1}) = (0.030 \text{ (s}^{-1}/\text{ppb)}) \times \Delta\text{NO}_2(\text{ppb}) \times \left( \frac{k_f([M], T)}{k_c([M], T)} \right) \quad (\text{S9})$$

284 where  $\Delta\text{NO}_2$  denotes the difference between the NO<sub>2</sub> concentrations in ambient air and zero gas (here  
 285 NO<sub>2</sub> is ~0.5 ppb in zero gas, which may be due to the interferences in zero gas), while  $k_f([M], T)$  and  
 286  $k_c([M], T)$  denote the rate constant calculated from the equations recommended by Sander et al. (2011)<sup>8</sup>  
 287 using the temperature in the reaction cell at the ambient air measurement time and calibration time,  
 288 respectively.

### 289 **Temperature and pressure influence correction**

290 Reaction in SR6 is favored by low-temperature and high-pressure conditions and is believed to play an  
 291 important role in the free troposphere and particularly the upper troposphere as it becomes cooler with  
 292 higher pressure<sup>9</sup>. The room temperature was maintained at 298 K during the whole campaign. However,  
 293 the temperature in the reaction cell ranged from 298 K to 302 K due to the sampled ambient air  
 294 temperature. The temperature and pressure correction was done according to the procedure adopted by  
 295 the National Aeronautics and Space Administration (NASA) data evaluation panel, as follows<sup>8</sup>:

$$296 \quad k_f([M], T) = \left[ \frac{k_0(T)[M]}{1 + \frac{k_0(T)[M]}{k_\infty(T)}} \right] 0.6 \left\{ 1 + \left[ \log_{10} \left( \frac{k_0(T)[M]}{k_\infty(T)} \right) \right]^2 \right\}^{-1} \quad (\text{S10})$$

297 where  $k_0(T)$  denotes the low-pressure-limiting rate constants, which can be calculated as:

$$298 \quad k_0(T) = k_0^{300} \left( \frac{T}{300} \right)^{-n} \text{ cm}^6 \text{ molecule}^{-2} \text{ s}^{-1} \quad (\text{S11})$$

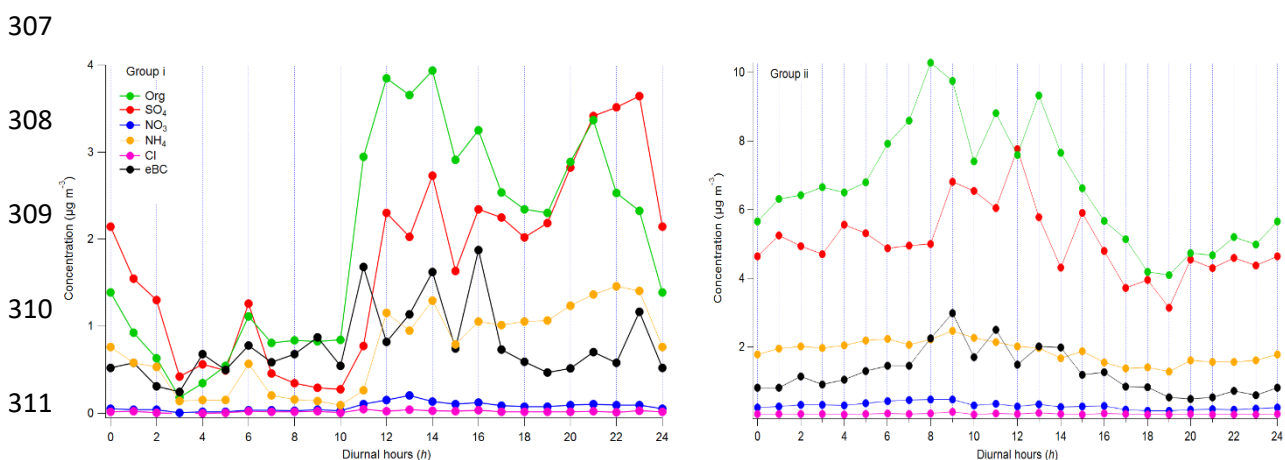
299 and  $k_\infty(T)$  denotes the limiting high-pressure rate constant, which can be calculated similarly:

$$300 \quad k_\infty(T) = k_\infty^{300} \left( \frac{T}{300} \right)^{-m} \text{ cm}^3 \text{ molecule}^{-1} \text{ s}^{-1} \quad (\text{S12})$$

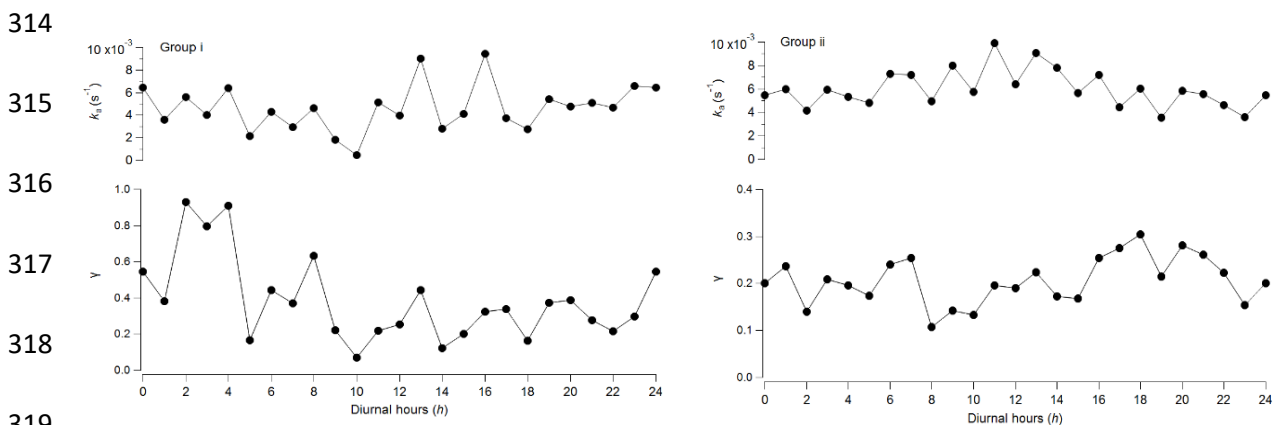
301 Here,  $n$  and  $m$  in Eqs. S11&S12 represent the temperature-dependent coefficients, which are  
 302 recommended as  $0.34 \pm 0.4$  and  $1.1 \pm 1.4$ , respectively. The equilibrium constants at temperature  $T$ ,  $K$   
 303 ( $T$ ), can be expressed as:

$$304 \quad K(T) = \frac{k_f([M], T)}{k_{-1}(T)} = 2.1 \times 10^{-27} \left( \frac{10900}{T} \right) \text{ cm}^3 \text{ molecule}^{-1} \text{ s}^{-1} \quad (\text{S13})$$

305 Thus,  $k_{-1}(T)$ , which is the rate constant of the reverse reaction of SR6, can be calculated from the  
 306 known  $K(T)$  and  $k_f([M], T)$ .

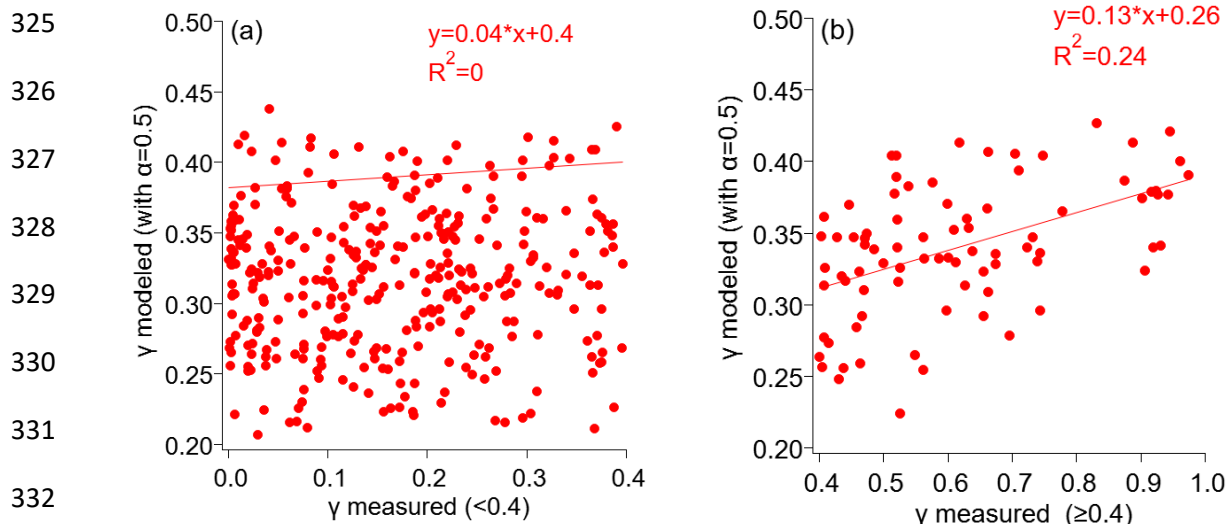


312 Figure S5: Diurnal trends in non-refractory chemical components plus eBC of group i (left side) and  
 313 group ii (right side).



320 Figure S6: Diurnal trends in total HO<sub>2</sub> reactivity caused by the ambient aerosol phase ( $k_a$ , upper panel)  
 321 and the HO<sub>2</sub> uptake coefficients onto ambient aerosols ( $\gamma$ , lower panel).

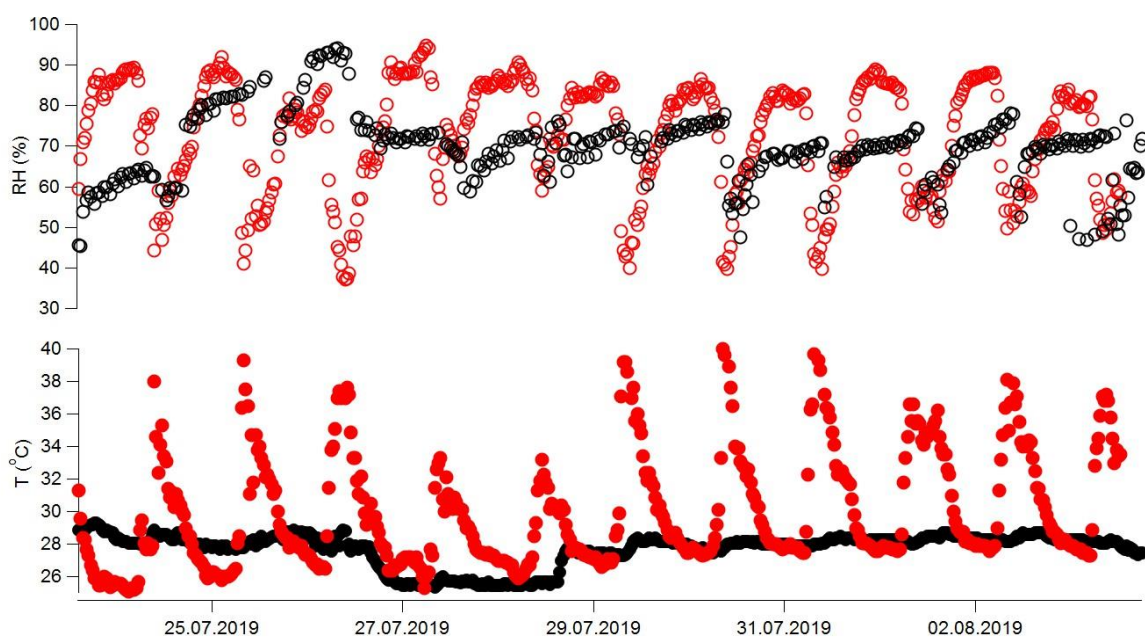
322  
 323  
 324



333 Figure S7: Correlations between measured and modeled  $\gamma$  with (a)  $\gamma < 0.4$  and (b)  $\gamma \geq 0.4$ .

334

335



336

337 Figure S8: Time series of the half-hour averaged ambient RH (red open cycles in the upper panel) and  
 338 temperature (red filled cycles in the lower panel) measurements in comparison to the reaction cell RH  
 339 (black open cycles in the upper panel) and temperature (black filled cycles in the lower panel).

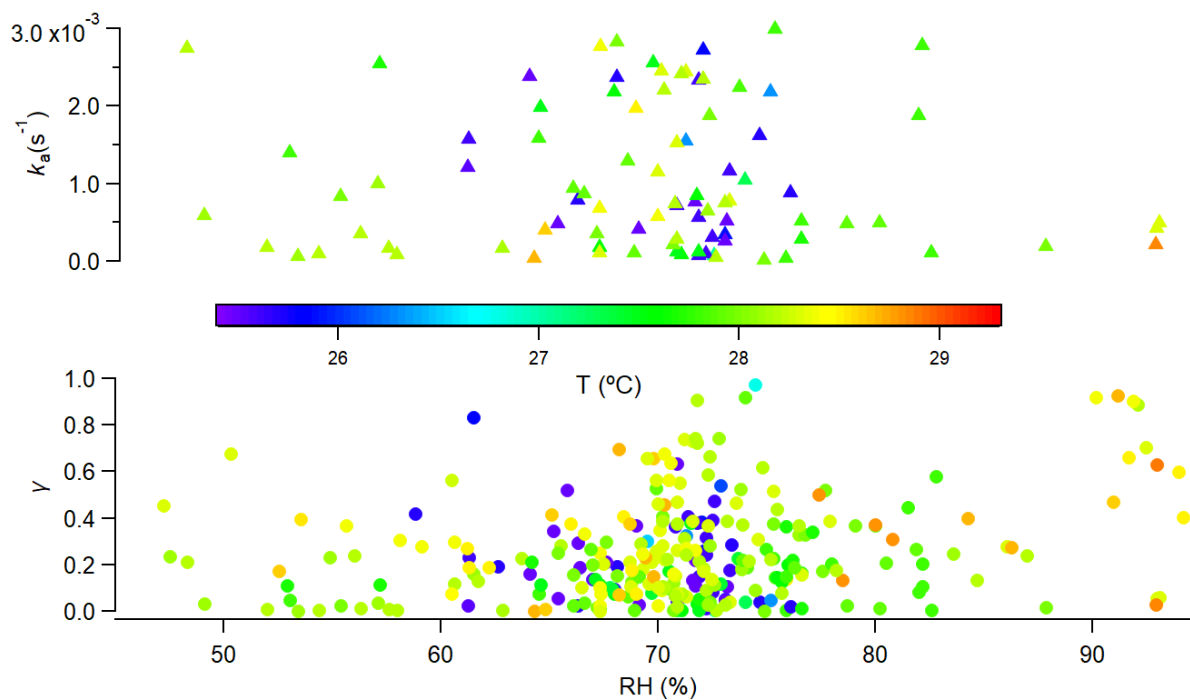
340

341

342

343

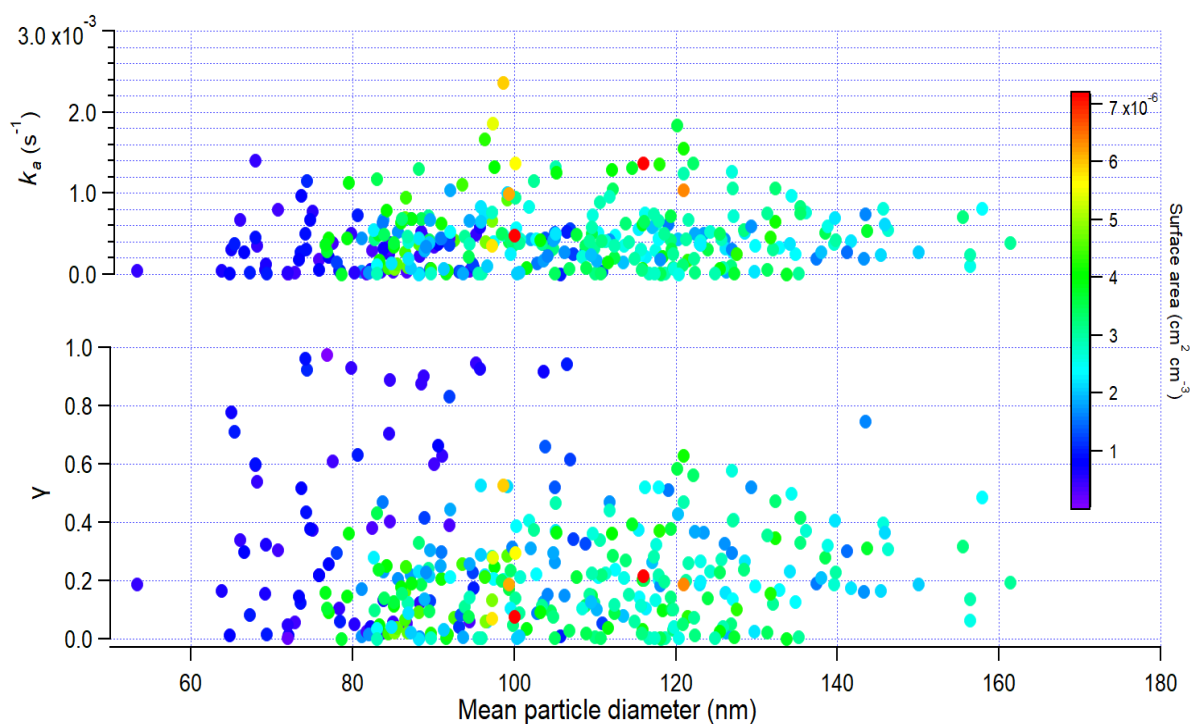
344



345

346 Figure S9:  $k_a$  and  $\gamma$  values as a function of RH in the reaction cell, colored coded with  $T$ .

347

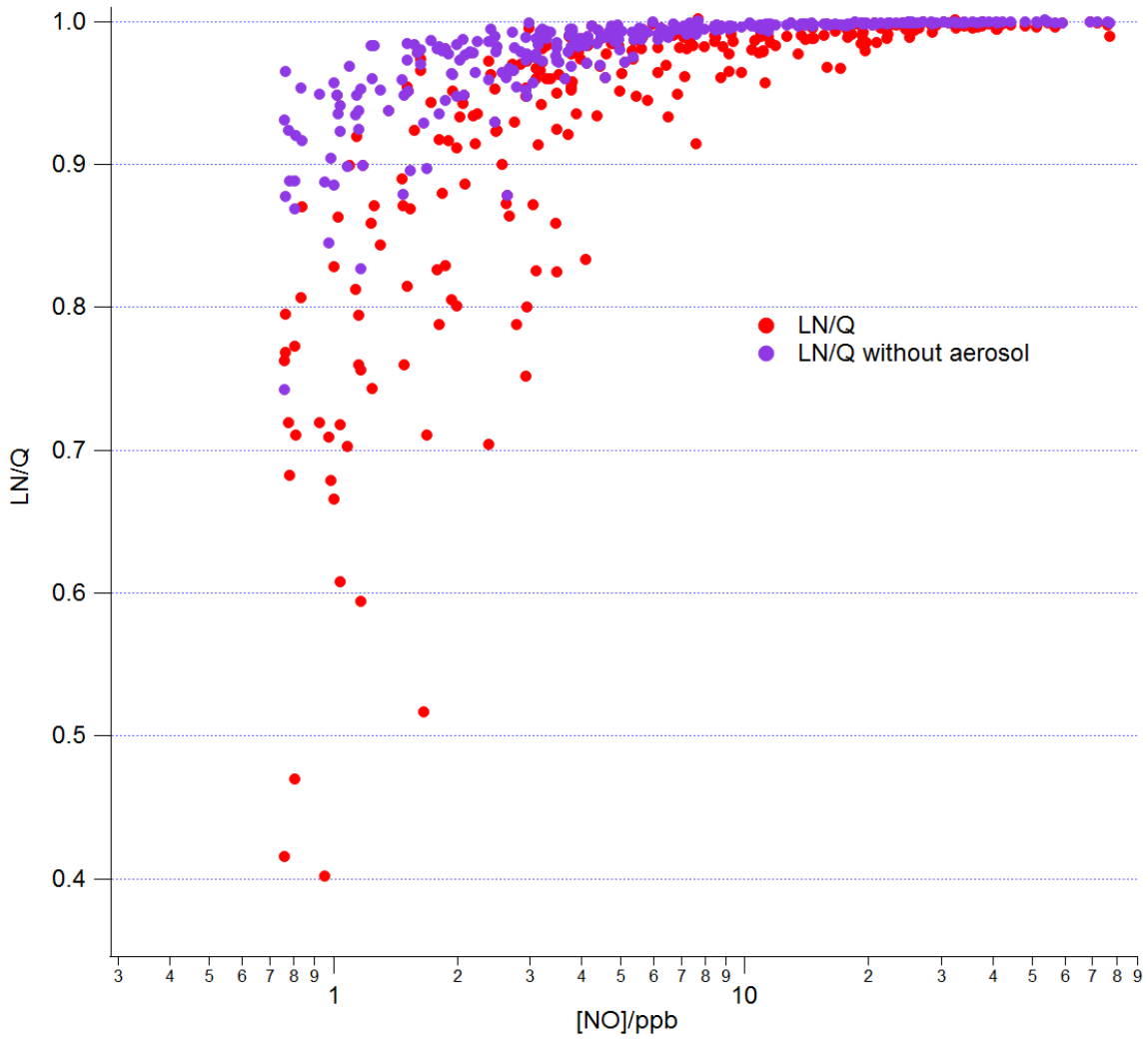


348

349 Figure S10:  $k_a$  (upper panel) and  $\gamma$  (lower panel) as a function of mean particle diameter, color coded  
 350 with the surface area concentration.

351

352

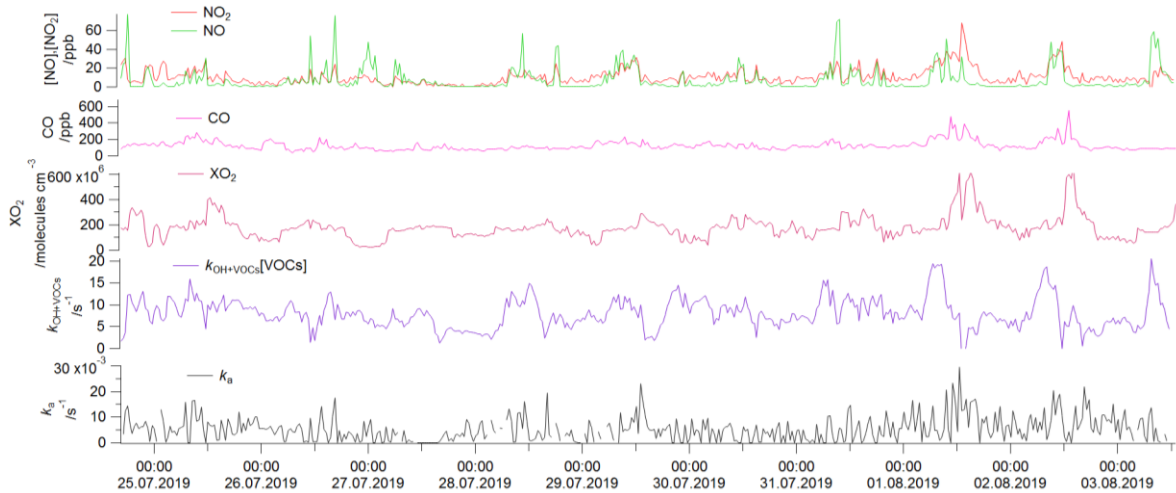


354

355 Figure S11: Dependence of day time LN/Q and LN/Q\_without\_aerosol on [NO].

356

357 **Profiles of key factors used in Section 3.5:**



358

359 Figure S12: Temporal variations in key factors in ambient air for determining XO<sub>2</sub> loss rates and  
 360 P(O<sub>3</sub>) sensitivity in Sect. 3.6.

361

362

363 **Table S1** Summary of equations and values used in Section 3.4.

Parameters	Equations and values	Ref.
$\omega / \text{cm s}^{-1}$	47376	
$\alpha^{\text{HO}_2^*}$	0.2 or 0.5	[10-17]
$H_{eff} / \text{M atm}^{-1}$	$H_{\text{HO}_2} (1 + \frac{k_{eq}}{[H^+]})$	[18]
$H_{\text{HO}_2} / \text{M atm}^{-1}$	$\text{EXP}(4.9 \times 4184 / (8.314 \times T))$	[19]
$k_{eq}^{**}$	$2.1 \times 10^{-5}$	[18]
$[H^+] / \text{mol L}^{-1}$	$10^{-\text{pH}}$	
pH	Calculated from the ISORROPIA-II model	
$R / \text{J mol}^{-1} \text{K}^{-1}$	8.314	
$[\text{HO}_2(\text{g})]^{***}$	$1.0 \times 10^{10}$	[3]
$r_p / \text{cm}$	Measured by SMPS	
$k_{\text{TMI}}^{\text{II}} / \text{M}^{-1} \text{s}^{-1}$	$10^9$	[18]
$[\text{TMI}] / \text{mol L}^{-1}$ (using $\text{Cu}^{2+}$ as surrogate) ****	$\frac{0.1 \times [\text{Cu}]^{***}}{\text{Liquid content in the aerosol}^{****}}$	[20]
$D_{aq}$	$10^{-5}$	[18]

364 \* Due to the aerosol particles collected in Yokohama City containing Cu, a high accommodation  
 365 coefficient of HO<sub>2</sub> ( $\alpha^{\text{HO}_2}$ ) may lead to HO<sub>2</sub> uptake as an important sink of the HOx radical. According  
 366 to the current research studies, we select  $\alpha^{\text{HO}_2}$  as 0.2 (typically for organics) and 0.5 (typically for  
 367 inorganics) for the model simulation.

368 \*\* HO<sub>2</sub> acid dissociation constant

369 \*\*\*HO<sub>2</sub> concentration in the reaction cell, calculated using the same method as Zhou et al. (2019)<sup>3</sup>.

370 \*\*\*\* Measured by off-line method

371

372

373

374

375

376

377 **Table S2** Summary of equations and values used in Section 3.6.

Parameters	Equations and values	Ref.
$k_a=k_{\text{HO}_2}=k_{\text{RO}_2}$	Observed	
$k_{\text{NO}-\text{XO}_2}=k_{\text{NO}-\text{HO}_2}=k_{\text{NO}-\text{RO}_2}$ /cm <sup>3</sup> molecule <sup>-1</sup> s <sup>-1</sup>	$3.3 \times 10^{12} \exp\left(\frac{270}{T}\right)$	[21]
[OH] /molecules cm <sup>-3</sup>	10 <sup>6</sup> (we assumed it is constant during the campaign)	
[HO <sub>2</sub> ]* /molecules cm <sup>-3</sup>	Day time (4:30 am – 7 pm): $\exp(8.4171 \times 10^{-13}[\text{O}_3]+18.081)$ Night-time (7 pm – 4:30 am): $6.042 \times 10^6 + 1.841 \times 10^{-4}[\text{O}_3]$	[22]
[XO <sub>2</sub> ]/molecules cm <sup>-3</sup>	[HO <sub>2</sub> ] plus [RO <sub>2</sub> ]	
[HCHO]**/ppb	2	
$k_{\text{OH}-\text{VOCs}}[\text{VOCs}]/\text{s}^{-1}$	Total OH reactivity ( $k_{\text{OH}}^*$ ) minus $k_{\text{OH}+\text{NO}_2}[\text{NO}_2]$	
$k_{\text{HO}_2-\text{HO}_2}$ /cm <sup>3</sup> molecule <sup>-1</sup> s <sup>-1</sup>	$1.5 \times 10^{-12}$	[23]
$k_{\text{HO}_2-\text{RO}_2}$ /cm <sup>3</sup> molecule <sup>-1</sup> s <sup>-1</sup>	$2.91 \times 10^{-13} \exp\left(\frac{1300}{T}\right) [1-\exp(-0.245n)]$ (n = 4, assumed from observed VOCs distribution).	[24]
$k_{\text{OH}-\text{HCHO}}$ /cm <sup>3</sup> molecule <sup>-1</sup> s <sup>-1</sup>	$8.2 \times 10^{-12} \times (T/298) \exp(0.33/(8.314 \times T))$	[8]
$k_{\text{OH}-\text{CO}}$ /cm <sup>3</sup> molecule <sup>-1</sup> s <sup>-1</sup>	$2.4 \times 10^{-13}$	[21]
$k_{\text{OH}-\text{NO}_2}$ /cm <sup>3</sup> molecule <sup>-1</sup> s <sup>-1</sup>	$1.21 \times 10^{-11}$	[25]

378 \*Measured in real time

379 \*\*Average value measured during the campaign

380

381

382

383

384

385

386

387

388

- 390 1. Sadanaga, Y.; Yoshino, A.; Watanabe, K.; Yoshioka, A.; Wakazono, Y.; Kanaya, Y.; Kajii, Y.,  
391 Development of a measurement system of OH reactivity in the atmosphere by using a laser-induced  
392 pump and probe technique. *Review of Scientific Instruments* **2004**, *75*, (8), 2648-2655.
- 393 2. Miyazaki, K.; Nakashima, Y.; Schoemaeker, C.; Fittschen, C.; Kajii, Y., Note: A laser-flash  
394 photolysis and laser-induced fluorescence detection technique for measuring total HO<sub>2</sub> reactivity in  
395 ambient air. *Review of Scientific Instruments* **2013**, *84*, (7), 076106.
- 396 3. Zhou, J.; Murano, K.; Kohno, N.; Sakamoto, Y.; Kajii, Y., Real-time quantification of the total  
397 HO<sub>2</sub> reactivity of ambient air and HO<sub>2</sub> uptake kinetics onto ambient aerosols in Kyoto (Japan).  
398 *Atmospheric Environment* **2019**, 117189.
- 399 4. Sakamoto, Y.; Zhou, J.; Kohno, N.; Nakagawa, M.; Hirokawa, J.; Kajii, Y., Kinetics study of OH  
400 uptake onto deliquesced NaCl particles by combining laser photolysis and laser-induced fluorescence.  
401 *The Journal of Physical Chemistry Letters* **2018**, *9*, (14), 4115-4119.
- 402 5. Sioutas, C.; Kim, S.; Chang, M., Development and evaluation of a prototype ultrafine particle  
403 concentrator. *Journal of Aerosol Science* **1999**, *30*, (8), 1001-1017.
- 404 6. Matthews, P. S. J.; Baeza-Romero, M. T.; Whalley, L. K.; Heard, D. E., Uptake of HO<sub>2</sub> radicals  
405 onto Arizona test dust particles using an aerosol flow tube. *Atmospheric Chemistry and Physics* **2014**,  
406 *14*, (14), 7397-7408.
- 407 7. Brown, R. L., *Tubular flow reactors with first-order kinetics*. 1978; Vol. 83.
- 408 8. Sander, S. P., J. Abbatt, J. R. Barker, J. B. Burkholder, R. R. Friedl, D. M. Golden, R. E. Huie, C. E.  
409 Kolb, M. J. Kurylo, G.; K. Moortgat, V. L. O. a. P. H. W., Chemical kinetics and photochemical data for  
410 use in atmospheric studies, Evaluation No. 17. *Jet Propulsion Laboratory publication* **2011**, *JPL*  
411 *Publication 10-6*, (Jet Propulsion Laboratory, Pasadena, 2011 <http://jpldataeval.jpl.nasa.gov>).
- 412 9. Chen, G.; Davis, D.; Crawford, J.; Hutterli, L. M.; Huey, L. G.; Slusher, D.; Mauldin, L.; Eisele, F.;  
413 Tanner, D.; Dibb, J.; Buhr, M.; McConnell, J.; Lefer, B.; Shetter, R.; Blake, D.; Song, C. H.; Lombardi, K.;  
414 Arnoldy, J., A reassessment of HO<sub>x</sub> South Pole chemistry based on observations recorded during ISCAT  
415 2000. *Atmospheric Environment* **2004**, *38*, (32), 5451-5461.
- 416 10. Lakey, P. S. J.; George, I. J.; Baeza-Romero, M. T.; Whalley, L. K.; Heard, D. E., Organics  
417 substantially reduce HO<sub>2</sub> uptake onto aerosols containing transition metal ions. *The Journal of Physical*  
418 *Chemistry A* **2016**, *120*, (9), 1421-1430.
- 419 11. Lakey, P. S. J.; Berkemeier, T.; Krapf, M.; Dommen, J.; Steimer, S. S.; Whalley, L. K.; Ingham, T.;  
420 Baeza-Romero, M. T.; Pöschl, U.; Shiraiwa, M.; Ammann, M.; Heard, D. E., The effect of viscosity and  
421 diffusion on the HO<sub>2</sub> uptake by sucrose and secondary organic aerosol particles. *Atmospheric*  
422 *Chemistry and Physics* **2016**, *16*, (20), 13035-13047.
- 423 12. Taketani, F.; Kanaya, Y.; Akimoto, H., Kinetics of heterogeneous reactions of HO<sub>2</sub> radical at  
424 ambient concentration levels with (NH<sub>4</sub>)<sub>2</sub>SO<sub>4</sub> and NaCl aerosol particles. *The Journal of Physical*  
425 *Chemistry A* **2008**, *112*, (11), 2370-2377.
- 426 13. Thornton, J.; Abbatt, J. P. D., Measurements of HO<sub>2</sub> uptake to aqueous aerosol: Mass  
427 accommodation coefficients and net reactive loss. **2005**, *110*, (D8).
- 428 14. Moon, D. R.; Taverna, G. S.; Anduix-Canto, C.; Ingham, T.; Chipperfield, M. P.; Seakins, P. W.;  
429 Baeza-Romero, M. T.; Heard, D. E., Heterogeneous reaction of HO<sub>2</sub> with airborne TiO<sub>2</sub> particles and its  
430 implication for climate change mitigation strategies. *Atmos. Chem. Phys.* **2018**, *18*, (1), 327-338.
- 431 15. George, I. J.; Matthews, P. S. J.; Whalley, L. K.; Brooks, B.; Goddard, A.; Baeza-Romero, M. T.;  
432 Heard, D. E., Measurements of uptake coefficients for heterogeneous loss of HO<sub>2</sub> onto submicron  
433 inorganic salt aerosols. *Physical Chemistry Chemical Physics* **2013**, *15*, (31), 12829-12845.
- 434 16. Taketani, F.; Kanaya, Y.; Akimoto, H., Heterogeneous loss of HO<sub>2</sub> by KCl, synthetic sea salt, and  
435 natural seawater aerosol particles. *Atmospheric Environment* **2009**, *43*, (9), 1660-1665.
- 436 17. Mozurkewich, M.; McMurry, P. H.; Gupta, A.; Calvert, J. G., Mass accommodation coefficient  
437 for HO<sub>2</sub> radicals on aqueous particles. *Journal of Geophysical Research: Atmospheres* **1987**, *92*, (D4),  
438 4163-4170.

- 439 18. Thornton, J. A.; Jaeglé, L.; McNeill, V. F., Assessing known pathways for HO<sub>2</sub> loss in aqueous  
440 atmospheric aerosols: Regional and global impacts on tropospheric oxidants. *Journal of Geophysical*  
441 *Research: Atmospheres* **2008**, *113*, (D5).
- 442 19. Hanson, D. R.; Burkholder, J. B.; Howard, C. J.; Ravishankara, A. R., Measurement of hydroxyl  
443 and hydroperoxy radical uptake coefficients on water and sulfuric acid surfaces. *The Journal of Physical*  
444 *Chemistry* **1992**, *96*, (12), 4979-4985.
- 445 20. Ross, H. B.; Noone, K. J., A numerical investigation of the destruction of peroxy radical by Cu  
446 ion catalysed reactions on atmospheric particles. *Journal of Atmospheric Chemistry* **1991**, *12*, (2), 121-  
447 136.
- 448 21. Burkholder, J. B. S., S. P.; Abbatt, J.; Barker, J. R.; Huie, R. E.; Kolb, C. E.; Kurylo, 205 M. J.; Orkin,  
449 V. L.; Wilmouth, D. M.; Wine, P. H., Chemical kinetics and photochemical data for use in atmospheric  
450 studies. *Evaluation No. 18. Jet Propulsion Laboratory: Pasadena, USA* **2015**,  
451 <https://jpldataeval.jpl.nasa.gov/>.
- 452 22. Kanaya, Y.; Cao, R.; Akimoto, H.; Fukuda, M.; Komazaki, Y.; Yokouchi, Y.; Koike, M.; Tanimoto,  
453 H.; Takegawa, N.; Kondo, Y., Urban photochemistry in central Tokyo: 1. Observed and modeled OH  
454 and HO<sub>2</sub> radical concentrations during the winter and summer of 2004. *Journal of Geophysical*  
455 *Research: Atmospheres* **2007**, *112*, (D21).
- 456 23. Kanno, N.; Tonokura, K.; Tezaki, A.; Koshi, M., Nitrogen- and water-broadening coefficient  
457 measurements in the A<sup>~</sup>2A' ← X<sup>~</sup>2A'' 000 – 000 band of HO<sub>2</sub> using high-resolution diode laser two-  
458 tone frequency modulation spectroscopy. *Journal of Molecular Spectroscopy* **2005**, *229*, (2), 193-197.
- 459 24. Saunders, S. M.; Jenkin, M. E.; Derwent, R. G.; Pilling, M. J., Protocol for the development of  
460 the Master Chemical Mechanism, MCM v3 (Part A): tropospheric degradation of non-aromatic volatile  
461 organic compounds. *Atmospheric Chemistry and Physics* **2003**, *3*, (1), 161-180.
- 462 25. Sadanaga, Y.; Kondo, S.; Hashimoto, K.; Kajii, Y., Measurement of the rate coefficient for the  
463 OH+NO<sub>2</sub> reaction under the atmospheric pressure: its humidity dependence. *Chemical Physics Letters*  
464 **2006**, *419*, (4), 474-478.

465